Solid Earth

Rock alteration at the post-Variscan nonconformity: implications for Carboniferous–Permian surface weathering versus burial diagenesis and paleoclimate evaluation

Fei Liang[1], Jun Niu[1,2], Adrian Linsel[1], Matthias Hinderer[1], Dirk Scheuvens[1], and Rainer Petschick[3]

[1]Material and Geosciences, Institute of Applied Geosciences, Technical University of Darmstadt, Darmstadt 64287, Germany
[2]Faculty of Petroleum, China University of Petroleum-Beijing, Karamay Campus, Karamay 834000, China
[3]Faculty of Geosciences and Geography, Goethe University Frankfurt, Frankfurt 60438, Germany

Correspondence: Jun Niu (niujunmm@outlook.com)

Abstract. A nonconformity refers to a hiatal surface located between metamorphic or igneous rocks and overlying sedimentary or volcanic rocks. These surfaces are key features with respect to understanding the relations among climate, lithosphere and tectonic movements during ancient times. In this study, the petrological, mineralogical and geochemical characteristics of Variscan basement rock as well as its overlying Permian volcano-sedimentary succession from a drill core in the Sprendlinger Horst, Germany, are analyzed by means of polarization microscopy, and environmental scanning electron microscope, X-Ray diffraction, X-ray fluorescence and inductively coupled plasma mass spectrometry analyses. In the gabbroic diorite of the basement, the intensity of micro- and macro-fractures increases towards the top, indicating an intense physical weathering. The overlying Permian volcanic rock is a basaltic andesite that shows less intense physical weathering compared with the gabbroic diorite. In both segments, secondary minerals are dominated by illite and a mixed-layer phase of illite and smectite (I–S). The corrected chemical index of alteration (CIA) and the plagioclase index of alteration (PIA) indicate an intermediate to unweathered degree in the gabbroic diorite and an extreme to unweathered degree in the basaltic andesite. The τ values for both basaltic andesite and gabbroic diorite indicate an abnormal enrichment of K, Rb and Cs that cannot be observed in the overlying Permian sedimentary rocks. Accompanying minerals such as adularia suggest subsequent overprint by (K-rich) fluids during burial diagenesis which promoted the conversion from smectite to illite. The

overall order of element depletion in both basaltic andesite and gabbroic diorite during the weathering process is as follows: large-ion lithophile elements (LILEs) > rare earth elements (REEs) > high-field-strength elements (HFSEs). Concerning the REEs, heavy rare earth elements (HREEs) are less depleted than light rare earth elements (LREEs). Our study shows that features of supergene physical and chemical paleo-weathering are well conserved at the post-Variscan nonconformity despite hypogene alteration. Both can be distinguished by characteristic minerals and geochemical indices. Based on these results, a new workflow to eliminate distractions for paleoclimate evaluation and evolution is developed.

1 Introduction

Nonconformities refer to contact surfaces between different lithologies in the geological record that were produced over long-lasting periods of non-deposition and/or erosion and are of paramount importance for the subdivision and correlation of stratigraphic successions (Catuneanu, 1996). They also largely control the geometry of reservoirs for oil, gas and water (Gardner, 1940). Moreover, nonconformities play a key role in understanding changes in past interactions of the atmosphere, hydrosphere and lithosphere as well as in elucidating driving mechanism for the adaption and evolution of life on Earth (Fedo et al., 1995; Nesbitt and Young, 1989; Panahi et al., 2000) According to Catuneanu (1996),

stratigraphic sequences and bounding surfaces are assigned to different orders based on their relative importance, which is also known as a sequence hierarchy.

Especially for continental nonconformities, the buried paleo-weathered surfaces provide an ideal opportunity to analyze the weathering and climate conditions during exposure (Jian et al., 2019; Zhou et al., 2017). This includes the alteration and deformation of minerals, such as changes in crystal morphology of primary and secondary minerals during the weathering process, which is also called supergene alteration (Borrelli et al., 2014). After the paleo-weathered surface has been covered by sediments or volcanic rocks, burial commences, leading to an increase in temperature and pressure as well as the passage of diagenetic fluids. This second overprint during deep burial diagenesis is called hypergene alteration and has to be carefully distinguished from the primary supergene alteration (Dill, 2010).

The widespread post-Variscan nonconformity represents an important first-order bounding surface within the central and western European strata. The nonconformity is a result of the denudation of the Variscan orogen which mainly took place from the late Carboniferous to the early Permian (Henk, 1995; McCann, 1999; McCann et al., 2006; Zeh and Brätz, 2004). Locally, however, the contact surface was overlain during the Triassic period. To date, the tectonic evolution in central Europe during post-Variscan times has been well studied (Matte, 1991; Ziegler et al., 2004). However, studies on weathering during the Permo-Carboniferous are fairly scarce. On the other hand, climate and paleoenvironmental conditions are well known from coal-bearing paralic and lacustrine sediments in the sub-Variscan foredeep and post-Variscan intramontane basins which indicate an overall aridification trend from humid conditions in the Westphalian to hyperarid conditions in the Guadalupian (Upper Rotliegend). From the Lopingian, the climate turned back to semiarid conditions (Roscher and Schneider, 2006).

For the reconstruction of the weathering conditions and the paleoclimate, fine-grained sediments such as siltstone or mudstone are usually investigated (Nesbitt and Young, 1982; Singer, 1988). However, caution is needed as these sediments may be multi-sourced, recycled, and/or overprinted during transport and sedimentation (Fedo et al., 1995; Jian et al., 2019). To avoid this, it is feasible to analyze the weathering profile of igneous or metamorphic rocks in the source area itself. With this approach, more accurate in situ information regarding the weathering conditions during a certain period can be acquired. This approach also applies to the diagenetic history of the rocks that are situated in direct proximity to the post-Variscan nonconformity (Dill, 2010). The Sprendlinger Horst (Hesse, Germany) is a key area in southwestern Germany for investigating the rock alteration processes at the post-Variscan nonconformity, as plutonic Variscan basement rocks in this area are widely covered by only a thin layer of Cisuralian volcano-sedimentary rocks and the contact surface has been penetrated by numerous drilling efforts (Kirsch et al., 1988).

For this study, we selected a representative drill core reaching from unweathered basement rock into the volcanic-sedimentary cover that was analyzed at high resolution, in particular near the nonconformity. This drill core allowed not only for the study of the alteration in Variscan basement rocks but also for the study of the subsequent alteration of overlying early Permian basalt. We carried out a detailed petrographical, mineralogical, and geochemical study and applied a new workflow to distinguish the supergene and hypogene alteration processes within a first-order nonconformity. The workflow is based on normalizing mineral types and geochemical weathering indices to un-overprinted conditions and quantifying the observed deviations. With corrected geochemical and mineral information of the weathered profile, the weathering and paleoclimatic condition as well as the alteration scenario were addressed.

2   Geological setting

The Variscan orogen in central Europe was formed due to the collision of the Gondwana and Laurussia mega-continents and intervening microplates, namely Avalonia and Armorica. The final assemblage of these continents led to the formation of Pangaea between ca. 360 and 320 Ma during the Carboniferous (Powell and Conaghan, 1973; Schulmann et al., 2014). Due to a southward-directed subduction of the oceanic lithosphere below the Armorica microplate, the so-called Mid-German Crystalline Zone (MGCZ) was formed as a magmatic arc at the northern margin of Armorica during the Early Carboniferous; as a highland, this region continuously weathered and eroded until thermal subsidence began to dominate in central Europe (von Seckendorff et al., 2004a; Willner et al., 1991; Zeh and Brätz, 2004; Zeh and Gerdes, 2010). As a consequence, the post-Variscan nonconformity was formed, which represents a diachronous time gap of multiple tens to hundreds of millions years in central Europe (Henk, 1995; Kroner et al., 2007; von Seckendorff et al., 2004b; Zeh and Brätz, 2004). The weathering surface was covered and, hence, preserved by Permian sedimentary or volcanic rocks summarized as the Rotliegend Group (Becker et al., 2012; Korsch and Schzfer, 1991; Stollhofen, 1998).

The Odenwald basement is the largest basement window of the MGCZ and consists of two major parts that are separated by the Otzberg shear zone: the Bergsträsser Odenwald in the west and the Böllstein Odenwald in the east (Zeh and Gerdes, 2010). The Bergsträsser Odenwald is subdivided into three tectonic units which are composed of magmatic and metamorphic rocks. These are, ordered from north to south, Unit I, which includes the gabbro-dioritic Frankenstein Complex; Unit II with the so-called Neunkirchen Magmatic Suite; and Unit III, which is dominated by large intrusive bodies of the Weschnitz, Heidelberg and Tromm plu-

tons (Dörr and Stein, 2019; Zeh and Will, 2008). The basement rocks of the so-called Cenozoic Sprendlinger Horst belong to Unit I and represent a northern extension of the Odenwald basement, consisting of amphibolite, granite, diorite, gabbroic diorite and gabbro. Geochronological investigations of crystalline rocks of Unit I yield an emplacement age of 362 ± 9 Ma for the Frankenstein gabbro (Kirsch et al., 1988). K/Ar and $^{40}Ar/^{39}Ar$ amphibole cooling ages fall into a range between 363 and 334 Ma (Kirsch et al., 1988; Schubert et al., 2001). Cooling below 350–300 °C (approximate closure temperature for the K–Ar system in biotite) occurred at about 330 Ma (Kirsch et al., 1988). Thermal modeling for the southern Bergsträsser Odenwald implies that the exhumation rate reached a maximum of 1.3 mm/a with average rates of 0.2 mm/a from 338 to 333 Ma (Henk, 1995). Recently, the basement rocks of Unit I of the Sprendlinger Horst were assigned to a Cadomian basement (Dörr and Stein, 2019). The Dieburg metagranite in this region was dated to 540 ± 8 Ma. According to these new findings, the investigated basement rocks are Cadomian relics in the Variscan orogen.

The Cenozoic Sprendlinger Horst constituted a structural barrier between the nearby Saar–Nahe Basin in the west and the Hessian Basin in the east from the early Cisuralian (McCann, 1999). In the Saar–Nahe Basin, a subsidence rate of approximately 0.26 mm/a has been revealed by backstripping analyses for the time between the Namurian and the Saxonian (Schäfer, 2011). The oldest sedimentary rocks of the Sprendlinger Horst are represented by the Moret Formation (Becker et al., 2012). The Permian Moret Formation deposited in an alluvial environment mostly in wadi-like systems that contain poorly sorted conglomerates, pelites, coarse-grained sandstones/wackes and breccias. The fluvial sedimentary rocks of the overlying Lower Langen Formation are interbedded with basalts and basaltic andesites. These volcanic rocks are the product of a Permo-Carboniferous volcanism which took place throughout central Europe. Ar^{40}/Ar^{39} dating of the volcanic products in the eastern Saar–Nahe Basin imply ages of around 290 ± 6 Ma (Lippolt and Hess, 1983). This age approximately corresponds to the age of the Donnersberg Formation (Schäfer, 2011). The volcanic products in the Sprendlinger Horst are correlated to this formation accordingly (Marell, 1989). Mudstone compaction rates indicate that over 3000 m of sediment was eroded due to the inversion of the basin structure during the mid- and later Permian (Henk, 1993).

During the Permo-Carboniferous, due to continental climate conditions within the supercontinent Pangaea, the paleoclimate in central Europe graduated from humid to hyperarid conditions (Parrish, 1993). In the Permian and Triassic, only the margins of the supercontinent attracted monsoonal rainfall and showed semiarid to subhumid conditions (Parrish, 1993, 1995). The overall aridization is superimposed by several wet phases, namely the Westphalian C/D, the Stephanian A (303.6 to 301.7 Ma), the Stephanian C to early lower Rotliegend (299.1 to 295.5 Ma) and the early upper Rotliegend I wet phase (291 to 287 Ma), respectively. These "wet phases" can be observed in the whole European region and are thought to be linked to deglaciation events of the Gondwana ice cap (Roscher and Schneider, 2006).

During the Mesozoic, the tectonic activity in central Europe was relatively low and was accompanied by continuous subsidence and marine transgression. In this phase, around 1500 m of sediment accumulated, which overlaid the Variscan basement and/or Permo-Carboniferous sediments and volcanic rocks (Timar-Geng et al., 2006). The maximum thickness of overburden is expected for the Jurassic (Schäfer, 2011). This is also the period of maximum heating and hydrothermal activity, which overprinted both the Variscan crystalline basement and the overlain sediments and volcanics locally. For this period, the formation of hydrothermal ores in central and southwest Germany is also well documented (Bons et al., 2014; Staude et al., 2011; Timar-Geng et al., 2004). Based on apatite fission track analysis in crystalline rocks of the Odenwald basement, Wagner et al. (1990) estimated temperatures of more than 130 °C for the Jurassic. Burisch et al. (2017) calculated homogenization temperatures from fluid inclusions in hydrothermal veins of 272–286 °C and 180 °C during the middle Jurassic and the Cretaceous, respectively. These temperatures can only be explained by higher heat flow and/or ascending hydrothermal fluids.

During the late Cretaceous and the Eocene, coupled with compressional intraplate stress of the Alpine Orogeny, the Upper Rhine Graben system was formed (Behrmann et al., 2005). In conjunction with the formation of the Upper Rhine Graben, the Sprendlinger Horst was formed. The latter is bounded by the Rhine Graben fault system in the west and by the Gersprenz Graben in the east. Most of the sediments that overlaid the post-Variscan crystalline basement in the research area have been eroded since the Cretaceous (Mezger et al., 2013; Schwarz and Henk, 2005). In the nearby southeastern Odenwald region, they are partly conserved and reach a thickness of 500 m for the Lower Triassic Buntsandstein (Marell, 1989). On the Sprendlinger Horst, only Permian volcano-sedimentary rocks remained which decrease in thickness from north to south of Darmstadt from 250 to 0 m (Marell, 1989; Mezger et al., 2013)

3 Materials and methods

Numerous drill cores in the Sprendlinger Horst were acquired by a scientific drilling project between 1996 and 2001. Many of the drill cores expose the post-Variscan nonconformity in shallow depths of up to 80 m below ground surface and, thus, provide a unique chance to investigate this paleo-surface at local scales. Along these drill cores, core GA1 was selected because it exposes three different lithological units, namely the plutonic basement at the bottom, the Permian volcanic lava in the middle and the overlying Permian

Rotliegend sedimentary rocks at the top. The sedimentary rocks show a gradual transition from alluvial facies at the base to fluvial facies at the top (Fig. 1) and mainly consist of matrix-rich breccias, wackes and siltstones. Both the top of the basement rock and the top of the volcanic lava constitute paleo-surfaces that faced intense alteration throughout their exposure, which is thought to be significantly shorter for the volcanic rocks. The macroscopic alteration underneath these surfaces is intense; this is expressed by a higher degree of fracturing, bleaching and grain disaggregation. The degree of macroscopic alteration decreases with increasing depth in these parts. The core offers the unique opportunity to study subsequent weathering intervals and to compare typical end-members of rock types with weak (gabbroic diorite) and strong (andesitic basalt) vulnerability to chemical weathering.

In total, 24 samples were extracted from the GA1 drill core: 11 belonged to the basement, 6 belonged to the overlying volcanic rock (Fig. 1) and 7 belonged to the sedimentary rocks of the Lower Langen Formation. In order to capture the small-scale petrographic and geochemical variations in the weathering zones appropriately, we reduced the sampling interval in the topmost part of the volcanic rock and in the basement to 40 cm; for the rest of the core, the interval was around 1 m in order to avoid the fractures.

The samples were used to prepare thin sections that were analyzed by polarization microscopy and SEM–EDX (scanning electron microscopy–energy dispersive X-Ray analysis) for their petrographic characteristics. For mineral composition, trace element and major element analyses, all samples were crushed and milled into a powder with a diameter of less than 63 µm. One part of the powder was examined by X-ray diffraction (XRD) at Goethe University Frankfurt for whole rock mineral composition. Careful back-loading of the powder preparation was utilized for XRD in order to reduced preferred orientation. Using a PANalytical X'Pert diffractometer equipped with a Bragg–Brentano goniometer (Copper beam), each sample was scanned at 40 kV and 30 mA for 2 h. The start angle was 2.5°, the end angle was 70.0° and a step size of 0.008° was applied. The time for each step was 50 s. The mineral-phase proportions were estimated by weighted XRD peak intensities after conversion with their typical reference intensity ratios (RIR), as found in the powder diffraction file (PDF-2 and PDF-4 of the International Centre of Diffraction Data: https://www.icdd.com/, last access: 12 June 2019; see Table 1) with MacDiff software (Petschick et al., 1996).

The powder samples were sent to the State Key Laboratory of Isotope Geochemistry, Guangzhou Institute of Geochemistry, Chinese Academy of Sciences, for the examination of major elements by X-ray fluorescence (XRF) and the examination of trace elements by inductively coupled plasma mass spectrometry (ICP-MS). Before XRF analysis, samples were roasted at 900° for 3 h and weighed before and after heating to measure the loss on ignition (LOI). Subsequently, 0.51–0.53 g of each sample was mixed (with a ratio of 1 : 8) with $Li_2B_4O_7$ and fused at 1150° in a Pt crucible to make a glass disk for XRF analysis.

For trace and rare earth element analysis, 40 mg of sample powder was weighed and placed into high-pressure-resistant Savillex Teflon beakers to which 0.8 mL 1 : 1 HNO_3, 0.8 mL HF and 0.5 mL 3N $HClO_4$ were added. The mixture was heated for 48 h at 100° and then evaporated. A total of 0.8 mL 1 : 1 HNO_3 was then added and heated at 100° for 12 h. Next, 0.8 mL HF and 0.5 mL 3N $HClO_4$ were added, and the beaker was sealed and moved into an oven with a temperature of 190° for 48 h to make sure that the sample was completely dissolved. The beakers were then opened, the solution was evaporated and 4 mL 4N HNO_3 was added. Following this, the beakers were sealed and moved into the oven which was set at a temperature of 170° for 4 h. Finally, the solution was diluted with 3 % HNO_3 until the weight of the solution was 250 times the weight of the sample. A total of 0.25 g of the solution was taken and diluted with 3 % HNO_3 to 2.00 g, mixed with 2.00 g Rh–Re internal standard solution and examined by ICP-MS. To monitor the analytical quality, international standards of GSR-1(granite), GSR-2(andesite) and GSR-3(basaltic andesite) were applied.

4 Results

4.1 Petrographic characteristics

4.1.1 Plutonic rock

The Variscan basement in drill core GA1 consists of a coarse-grained plutonic rock with a conspicuous salt-and-pepper appearance and a phaneritic texture. Fractures are pervasive from 20.6 to 21.4 and from 21.7 to 22.3 m. The width of the fractures is around 1 cm. From 22.3 to 23.4 m, both fracture density and width gradually reduce downwards. Nearly all fractures are filled by secondary minerals (Fig. S1). Under the microscope, the fresh parts of the plutonic basement rock mainly consist of plagioclase (oligoclase and labradorite), quartz, biotite and amphibole (Fig. 2a). With decreasing depth, primary minerals such as plagioclase and biotite were gradually altered and transformed into secondary minerals; fractures are also ubiquitous in the thin sections in the topmost part. Primary grain shapes are distorted and most of them are filled with calcite (Fig. 2b). Moreover, recrystallized quartz coupled with calcite is found filled in the fractures (Fig. 2c). Some of the fractures are filled by dolomite accompanied with quartz (Fig. 2d). Even in the topmost part (20.6 m), the plagioclase grains are only partly altered (Fig. 2e).

4.1.2 Lava

The lava has a phaneritic, amygdaloidal texture. Fractures in this part are very limited and occur between 13.8 and
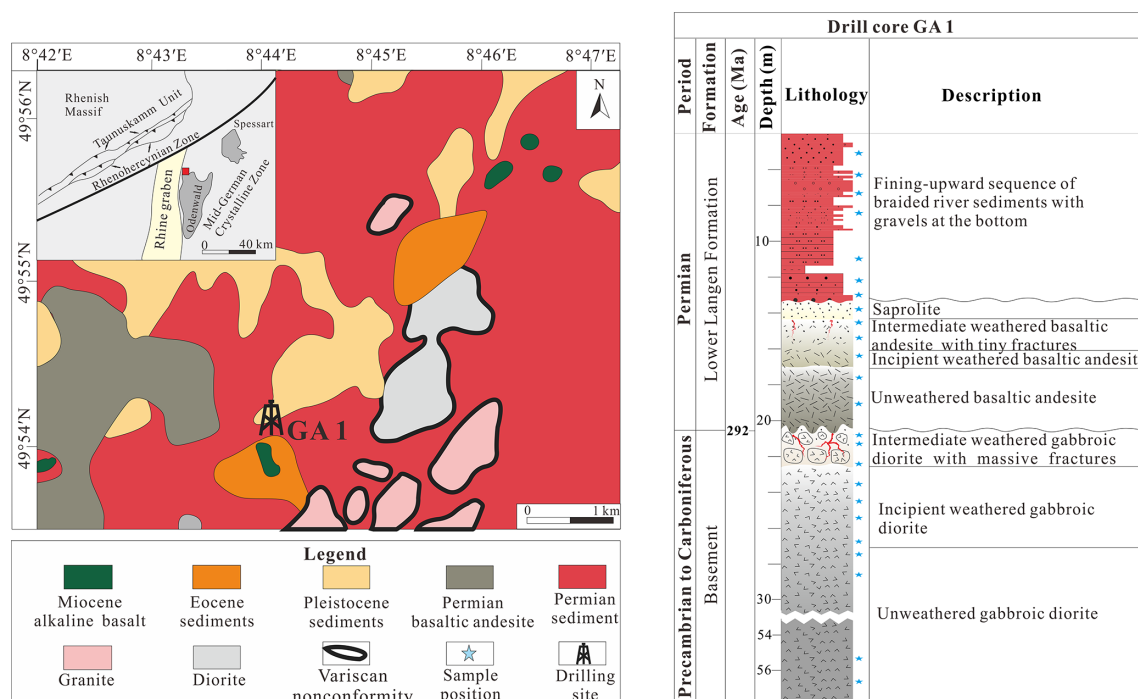
Figure 1. Location and geology of the research area, and the lithological section of the GA1 drill core; note the gap between 30 and 54 m drilling depth. Blue stars indicate the sampling locations.

14.7 m with a high angle to the horizon. The width is less than 1 mm, and the fractures are also filled with secondary minerals (Fig. S1). The fresh part of the volcanic rock mainly consists of plagioclase (albite) crystals and amygdaloid bodies that are made up of calcite and zeolite locally accompanied with chalcedony (Fig. 2f). With a decrease in depth, the content of plagioclase gradually decreases under the microscope. However, the thin section in the topmost part of the lava (13.9 m) shows a sudden change compared with the samples from lower parts. Here, nearly all primary minerals were altered to secondary clay minerals, but the primary grain shapes are still relatively intact (Fig. 2g). Some residual grains consist of a kaolinite rim and a core of illite or illite–smectite (I–S) mixed layers (Fig. 2h). In the void, adularia with kaolinite can be observed (Fig. 2i).

4.2 Mineral composition

4.2.1 Plutonic rock

The XRD results are listed in the Supplement (Table S1) and are plotted in Fig. 3. The plutonic basement part is composed of plagioclase (oligoclase and labradorite), K-feldspar (only in one sample), quartz, amphibole (mainly Mg-hornblende) and mica phases, with secondary minerals of illite (not separable from micas), vermiculite, I–S mixed layers, minor kaolinite, anatase, hematite, calcite and dolomite. Amphibole abundance decreases in the middle section and disappears in the uppermost part. In the topmost portion (20.6–23.5 m),

amphibole is not found. Furthermore, plagioclase decreases in abundance from around 40 % at the bottom to about 8 % at the top. Considering the mineralogical composition of the fresher parts of the plutonic rock, based on the quartz, alkali feldspar, plagioclase, feldspathoid (QAPF) diagram for plutonic rocks, the protolith of the basement rock can be classified as a quartz diorite/tonalite (Fig. S2), which corresponds well with Mezger et al. (2013).

4.2.2 Lava

The fresh samples of the volcanic rock are composed of augitic pyroxene and plagioclase (albite). In the weathered part, most of the phases appear as secondary minerals, such as quartz, hematite and anatase; clay minerals, such as illite, mixed layer illite-smectite (I–S), vermiculite and kaolinite; and carbonate minerals, like calcite and minor dolomite. The uppermost part of the lava is dominated by I–S mixed-layer minerals, the plagioclase content is less than 5 % and pyroxene is absent. The abundance of plagioclase (and pyroxene) gradually decreases from bottom to top, and illite and vermiculite exhibit an increasing tendency (Fig. 3). Based on the QAPF diagram for volcanic rocks, the protolith of the weathered volcanic rock can be classified as a basalt or andesite (Fig. S2).
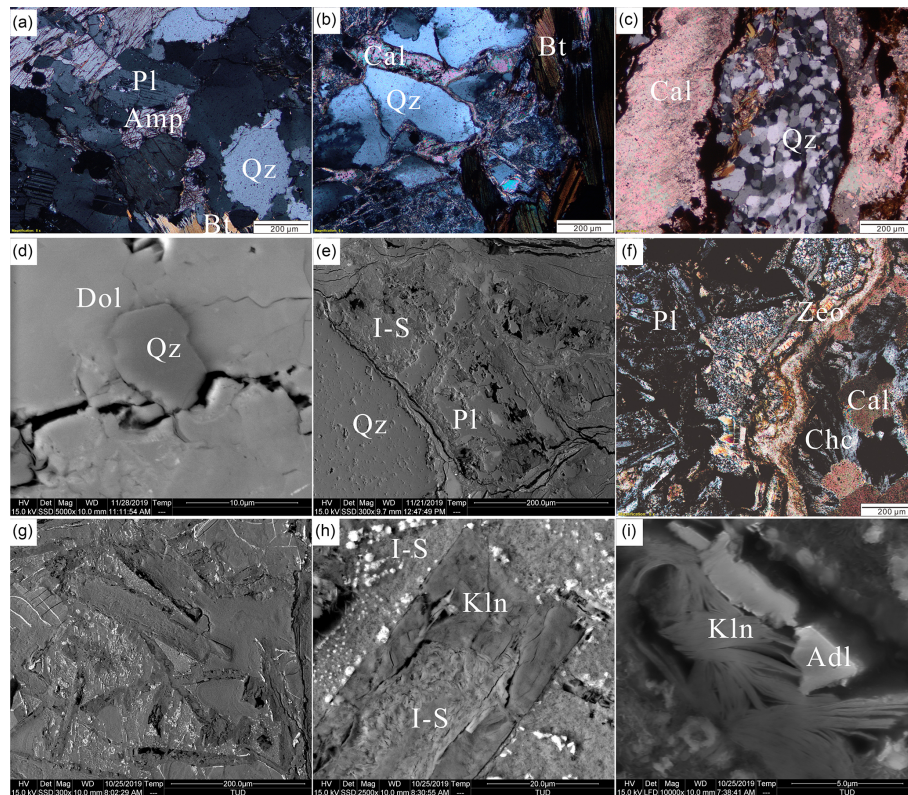
Figure 2. Petrographic characteristic of the basement and the overlying volcanic rock in the GA1 drill core: **(a)** fresh gabbroic diorite (PM, $z = 55.5$ m); **(b)** gabbroic diorite (PM, $z = 20.6$ m) and fractured quartz grain; **(c)** gabbroic diorite (PM, $z = 23.5$ m) and recrystallized quartz coupled with a calcite filled in fracture; **(d)** gabbroic diorite (BSE, $z = 21.5$ m) and dolomite accompanied by quartz; **(e)** gabbroic diorite (BSE, $z = 20.6$ m) and partly weathered plagioclase. **(f)** basaltic andesite (PM, $z = 17.8$ m) and fresh plagioclase grains with the amygdaloid consisting of calcite and zeolite and chalcedony; **(g)** basaltic andesite (BSE, $z = 13.9$ m) secondary clay minerals with intact primary grain shapes; **(h)** basaltic andesite (BSE, $z = 13.9$ m) and I–S surrounded by kaolinite within one residual plagioclase grain shape; **(i)** basaltic andesite (SEM, $z = 13.9$ m) with kaolinite and adularia filled in the void. The abbreviations used in the figure and caption are as follows: PM – polarizing microscopy, z – depth below ground surface, Amp – amphibole, Kln – kaolinite, Adl – adularia, Bt – biotite, Cal – calcite, Pl – plagioclase, Zeo – zeolite, Chc – chalcedony, Dol – dolomite and Qz – quartz.

4.3 Geochemical characteristics

4.3.1 Geochemical rock classification

In order to further verify the lithological type of the plutonic and volcanic rock for the basement part of the GA1 drill core, the geochemical data from comparatively fresh samples (23.5–56.5 m) are plotted in the total alkali silica (TAS) diagram (Middlemost, 1994) (Fig. 4). Here, the results mainly plot in the gabbroic diorite field (Fig. 4a), which is grossly consistent with the results from the petrographic classification (Fig. S2). For the volcanic rock classification, a revised Winchester–Floyd diagram is applied, which is based on immobile trace elements (Pearce, 1996). Most lava samples fall into the andesite/basaltic andesite field (Fig. 4b), which is also in accordance with the petrographic classification result. In the following, we use the result of chemical classification and term the two protolith rocks as gabbroic diorite and basaltic andesite.

4.3.2 Major elements

The concentrations of major elements are listed in the Supplement (Table S2) and are visualized in 1-D profiles for both basaltic andesite (Fig. 5a) and gabbroic diorite (Fig. 5b). Within the lower relatively fresh part of the gabbroic diorite, major elements such as K_2O, Na_2O, P_2O_5 CaO and MnO are almost constant. Al_2O_3 and TiO_2 fluctuate in the topmost part (20.6–21.5 m) and show an overall slightly increasing tendency from top to bottom. For Fe_2O_3, the fluctuation is high in the topmost part and low in the lower part. There is a sharp shift in most concentrations when approaching the intensely altered part at the top of the profile. Despite the high fluctuation in most concentrations in the uppermost part, a significant increase in K_2O and decrease in Na_2O are observed from bottom to top (Fig. 5b).

Concerning the basaltic andesite, there are some clear trends with increasing Al_2O_3, K_2O, P_2O_5 and TiO_2 concentrations and with decreasing CaO and Na_2O concentrations
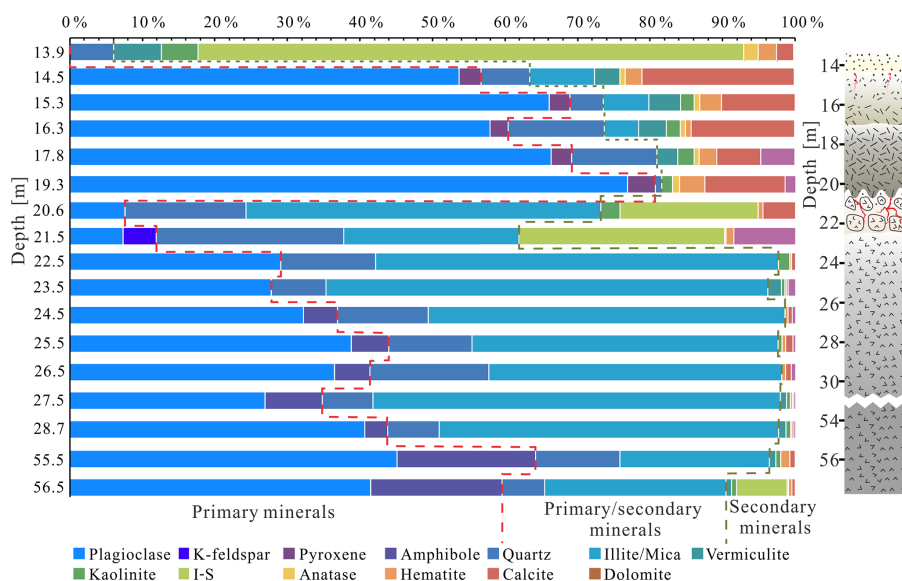
Figure 3. Mineral compositions of both Permian volcanic lava and Paleozoic basement rock in the GA1 drill core (measured by powder XRD).
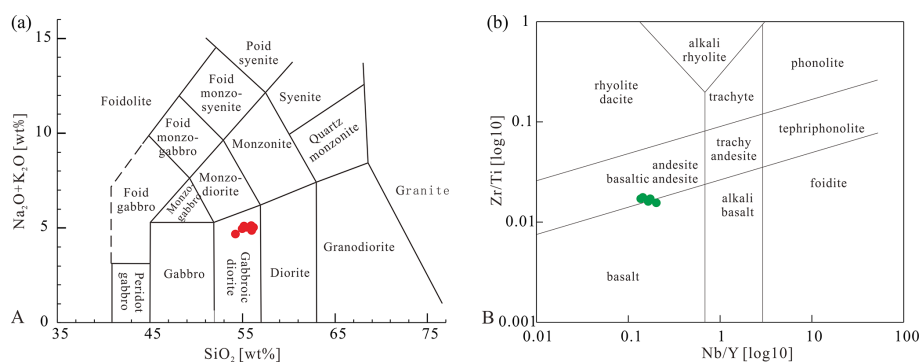
Figure 4. Classification of rocks of the GA1 well with a TAS diagram and revised Winchester–Floyd diagram: **(a)** samples from fresh and sufficiently fresh parts of the basement; **(b)** samples from overlain lava.

towards the top. In contrast to the gabbroic diorite, a sharp shift in concentrations is observed in the uppermost sample for all elements except for Fe_2O_3 which fluctuates along the profile (Fig. 5a).

4.3.3 Trace elements

Trace element data are also given in the Supplement (Table S3). Variations in representative trace elements from both gabbroic diorite and basaltic andesite are shown in Fig. 6. In the gabbroic diorite, except for the topmost part, fluctuations in high-field-strength elements (HFSEs) such as Zr, Hf, Nb, Ta and Th (in parts per million, ppm) are limited or even constant. For large-ion lithophile elements (LILEs), Rb and Cs decrease from top to the bottom, whereas Sr increases from 61 to 348 ppm. Ba fluctuates in the upper part of the gabbroic diorite section but is almost constant in the lower part.

Concerning the basaltic andesite part, HFSEs such as Zr, Hf, Nb, Ta and Th (in ppm) all exhibit an increasing tendency from the bottom to the top, with a sharp increase in the topmost sample. LILEs such as Rb and Cs also show an increasing tendency, whereas Sr reveals an inverse trend, with a decrease from 123 ppm at the bottom to 47 ppm in the topmost part. The tendency for Ba is irregular compared with the other elements, but the overall trend is decreasing.

4.3.4 Rare earth elements (REEs)

REE concentrations are listed in the Supplement (Table S4) and are shown as chondrite-normalized patterns (McDonough and Sun, 1995) in Fig. 7. The calculation for the anomalies of cerium (Ce) and europium (Eu) are defined as follows:

$$\frac{Ce}{Ce^*} = \frac{2 \times Ce_N}{La_N + Pr_N}, \tag{1}$$
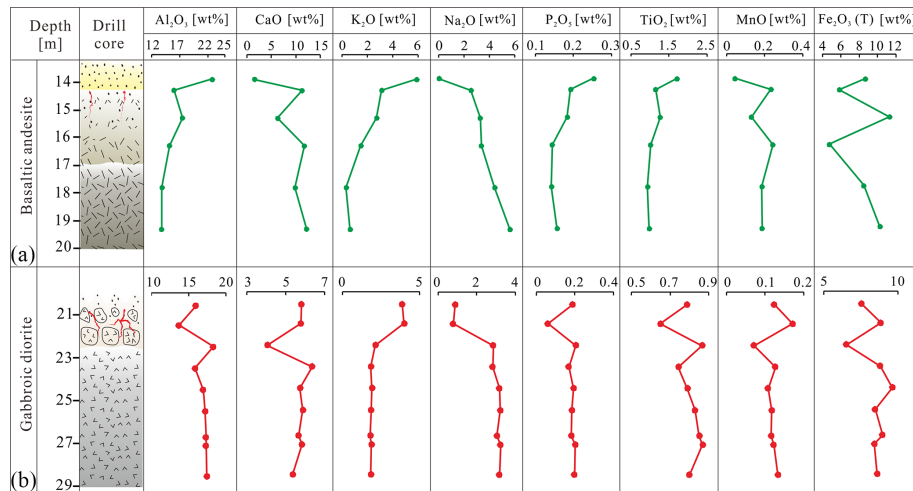
Figure 5. Major element content (in wt %) of the basaltic andesite **(a)** and the gabbroic diorite **(b)** along the drill core profile.
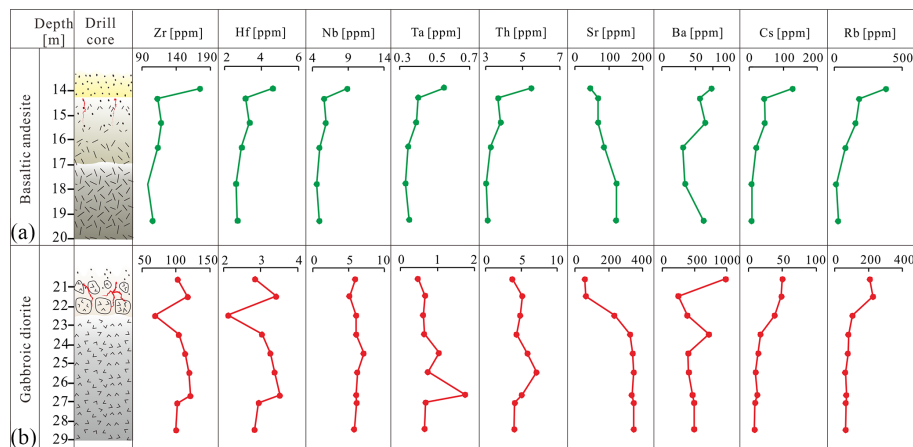
Figure 6. Representative trace element content (in ppm) of basaltic andesite **(a)** and gabbroic diorite **(b)** along the drill core profile.

and

$$\frac{Eu}{Eu^*} = \frac{2 \times Eu_N}{(Sm_N + Gd_N)}. \tag{2}$$

Here, Ce* and Eu* are the hypothetical concentrations of trivalent Ce and Eu, and X_N represents the normalized value of the element X. The distribution patterns of both gabbroic diorite and basaltic andesite are nearly parallel at different depths and exhibit decreasing values from the bottom to the top (Fig. 7). All samples are moderately enriched in light rare earth elements (LREEs) and have gently right-dipping REE patterns. They exhibit no Ce anomalies and slightly negative Eu anomalies.

5   Discussion

5.1   Chemical alteration

During chemical weathering, alkalis and alkaline earth elements contained in silicates such as feldspar, mica minerals, pyroxene and amphibole will be gradually depleted, whereas aluminum tends to remain in situ, generating clay minerals (Clift et al., 2014; Nesbitt and Young, 1982; Vázquez et al., 2016). Based on this mechanism, different types of weathering indices were developed to evaluate the weathering intensity. Among these, the chemical index of alteration (CIA) and the plagioclase index of alteration (PIA) were proposed by Nesbitt and Young (1982) and Fedo et al. (1995), respectively. They are defined as

$$CIA = \frac{Al_2O_3}{Al_2O_3 + CaO^* + Na_2O + K_2O} \times 100, \tag{3}$$
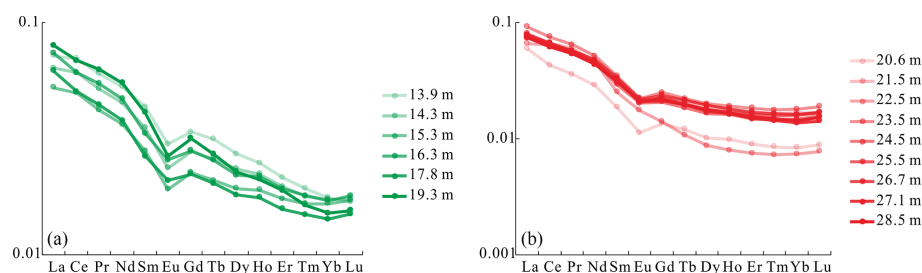
Figure 7. The REE pattern of basaltic andesite (a) and gabbroic diorite (b) at different depths.

and

$$PIA = \frac{Al_2O_3 - K_2O}{Al_2O_3 + CaO^* + Na_2O - K_2O} \times 100, \quad (4)$$

respectively. Here, all portions are given in molecular weight, and (in both equations) CaO* is the Ca content within silicate minerals only. Bulk rock analysis of altered rocks, however, is affected by Ca mobilization and secondary calcite precipitation. First, Ca may be transferred downward during weathering in the top part and may precipitate there along fractures that were formed before by physical weathering and/or rock relaxation. Second, Ca may be transferred by fluids from underlying or overlying formations during the burial process, depending on the hydraulic conditions. Both cases will increase the Ca content. Hence, bulk geochemistry cannot be applied directly. For the correction of calcitic CaO*, McLennan (1993) used the following approach: $CaO_{rest} = CaO - P_2O_5 * 10/3$, where P_2O_5 is related to apatite, and $CaO^* = CaO_{rest}$ when $CaO_{rest} < Na_2O$ or $CaO^* = Na_2O$ otherwise. With this calculation, the CIA value for fresh feldspar is about 50, unaltered basaltic andesite is between 30 and 45, granitoids range between 45 and 55, illite is from 75 to 85, muscovite yields a value of 75, and kaolinite and chlorite have the highest value of nearly 100 (Fedo et al., 1995). As a modification of the CIA, the PIA value for fresh rock is around 50, whereas for clay minerals such as kaolinite, illite and gibbsite, it is close to 100 (Fedo et al., 1995; Patino et al., 2003).

In our case, the CIA and PIA decrease from top to bottom for both gabbroic diorite and basaltic andesite. The PIA values are clearly higher than the CIA values (Fig. 8a). In the topmost basaltic andesite part, the CIA is up to 77, which indicates an intermediate degree of weathering. The results from XRD and backscattered electron microscopy (BSE), however, indicate that the plagioclase is weathered and 74 % of the constituent is I–S. This is well expressed by the PIA, which yields a value of 98; hence, the PIA is more consistent with the mineralogical and petrographic character than the CIA.

To better evaluate the weathering intensity, an A–CN–K ternary diagram is applied (Fedo et al., 1995; Nesbitt and Young, 1984). The letter A stands for Al_2O_3, CN stands for $(CaO^* + Na_2O)$ and K stands for the content of K_2O – all in

molecular proportions. The ideal weathering trend for different types of parent rocks in the upper continental crust should be parallel to the A–CN axis, but the original data tend to deviate from the theoretical weathering trend due to diagenetic alteration (Babechuk et al., 2015; Fedo et al., 1995; Zhou et al., 2017). The trends for both basaltic andesite and gabbroic diorite samples uniformly deviate from the ideal weathering tendency and excurse to the K apex (Fig. 8a), which clearly indicates a relative K enrichment. In the literature, the enrichment of K is interpreted as K metasomatism due to conversion among clay minerals, such as the transformation from kaolinite to illite or from plagioclase to K-feldspar (Fedo et al., 1995; Nesbitt and Young, 1984; Zhou et al., 2017). K metasomatism results in a lower CIA value relative to the actual weathering intensity and can also explain the deviation from the PIA. To address this problem, Fedo et al. (1995) suggested that the proportion of "pre-metasomatic" compositions of the weathering products could be determined by correcting each point on the A–CN–K diagram back to its predicted position. The method proposed by Panahi et al. (2000) for the K correction is applied as follows:

$$K_2O_{corr} = \frac{m * A_w + m * CN_w}{1 - m}. \quad (5)$$

Here, A_w and CN_w refer to the Al_2O_3 and $(CaO^* + Na_2O)$ content in the weathering zone, respectively, where

$$m = \frac{K}{A + CN + K}. \quad (6)$$

The K, A and CN values for the calculation of m were taken from the protolith sample.

With corrected K_2O values, the trend of all sample points in the A–CN–K diagram is parallel to the A–CN axis (Fig. 8b). Moreover, the CIA_{corr} values are now consistent with the PIA value. The CIA_{corr} values of the gabbroic diorite indicate an intermediate to incipient chemical weathering degree, with CIA_{corr} values of 80 in the top part and values of 58 at the bottom (Fig. 8b). PIA values decrease from 83 to 59 (Fig. 8b). For both the CIA_{corr} and PIA values, inconsistent trends between the topmost part (20.6–21.5 m) and the remaining section (22.5–28.5 m) result from a sudden decrease in the weathering degree which forms a "discontinuity". The CIA_{corr} and PIA values in the topmost part range from 79
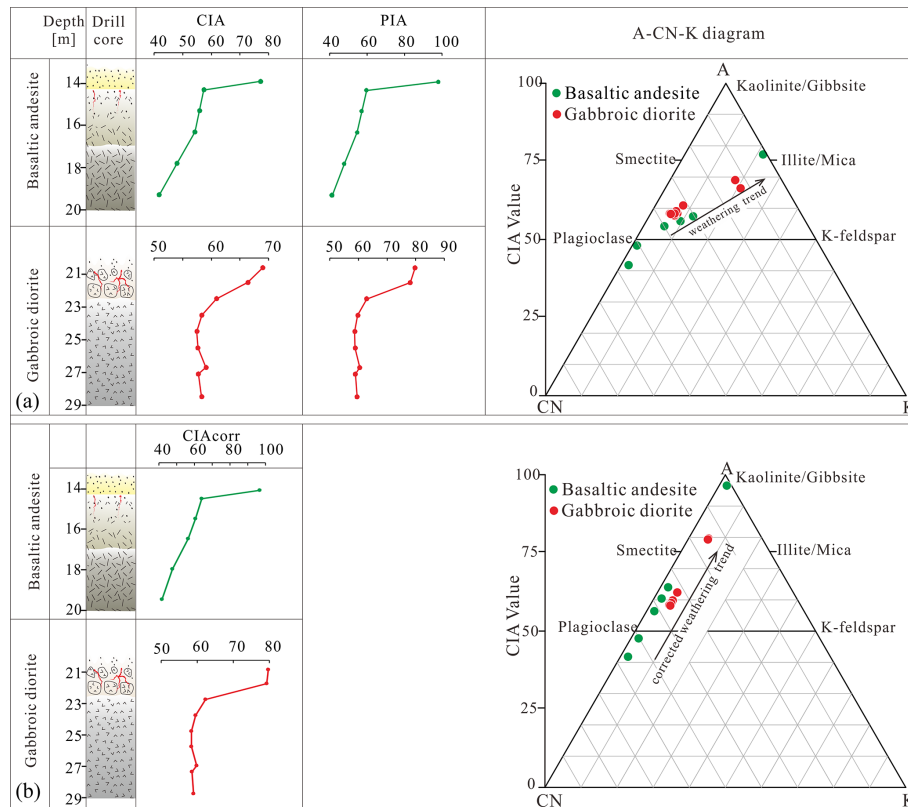
Figure 8. Weathering indices with an A–CN–K diagram of both basaltic andesite and gabbroic diorite before and after K correction, based on Fedo et al. (1995) and Nesbitt and Markovics (1997).

to 80 and from 78 to 80, respectively; in the remaining section, the CIA_{corr} and PIA values decrease from 62 to 58 and from 63 to 59, respectively. Petrographic and mineralogical features correspond well to the corrected weathering indexes. Secondary alteration products are mainly illite, with a small quantity of kaolinite and vermiculite.

The corrected CIA values in the basaltic andesite suggest an extreme to incipient weathering degree, with the CIA_{corr} and PIA decreasing from respective values of 97 and 98 at the top to respective values of 42 and 41 at the bottom. Similar to the gabbroic diorite, a discontinuity exists between the topmost part (13.9 m) and the lower part (14.3–19.3 m) for both CIA_{corr} and PIA values. The high CIA_{corr} and PIA values in the topmost part of the basaltic andesite indicate extreme chemical weathering. In the lower part of the basaltic andesite, the CIA_{corr} and PIA values decrease from 64 at the top to 42 at the bottom and from 65 at the top to 41 at the bottom, respectively (Fig. 8b). These values are much lower than values from the topmost part and suggest an incipient weathering degree. Based on the XRD results, the plagioclase content at the bottom is 77 % and declines gradually up the section to 54 % at 14.5 m before it suddenly drops to 0 % at 13.9 m. At a depth of 14.5 m, the plagioclase grains are still mostly fresh, which is clearly different from the uppermost 0.5 m in which they are completely altered.

5.2 Quantification of element transfer

For quantification of element transfer due to weathering and diagenesis, the τ model is applied (Anderson et al., 2002; Nesbitt, 1979; Nesbitt and Markovics, 1997). The model uses the relation of the mobile element concentration in the sample (M_{sample}) vs. the protolith ($M_{protolith}$) and between the immobile element concentration in the sample (I_{sample}) vs. the protolith ($I_{protolith}$). Among the immobile elements, Ti is widely used as a key element (Middelburg et al., 1988). Thus, the model is defined as follows:

$$\tau_M = \frac{M_{sample} \times Ti_{protolith}}{M_{protolith} \times Ti_{sample}} - 1. \tag{7}$$

When $\tau_M > 0$, element M is enriched during alteration; when $\tau_M = 0$, element M is immobile during alteration; when $0 > \tau_M > -1$, element M is depleted; when $\tau_M = -1$, element M is completely lost from the material. For the basaltic andesite and gabbroic diorite, the samples from the bottom (19.3 m for basaltic andesite and 55.5 and 56.5 m for gabbroic diorite) were selected as protoliths to provide the lowest degree of alteration based on the CIA values, petrographic features and XRD results.

The results for major and trace elements are listed in the Supplement (Table 5) and are plotted in Fig. 9. In the basaltic
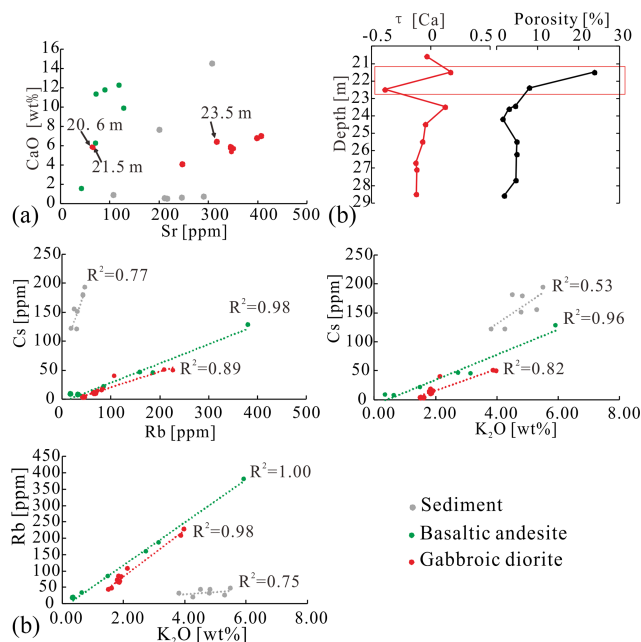
Figure 9. Element characteristics: **(a)** Sr–CaO cross-plot for the GA1 drill core; **(b)** relationship between the τ value and the porosity in the gabbroic diorite; **(c)** relationship among Rb, Cs and K_2O for sedimentary rocks, basaltic andesite and gabbroic diorite.

andesite part, both Ca and Na are strongly depleted in the topmost section (13.9 m), with τ_{Ca} and τ_{Na} of -0.93 and -0.99, respectively. τ_{Ca} gradually increases from -0.60 to -0.07 and τ_{Na} increases from -0.60 to -0.18 with increasing depth from 14.3 m down to 17.8 m. The discontinuity between the topmost part and the remaining section corresponds well to the CIA and PIA values. However, the τ_{Na} values from the top gradually increase from -0.70 (20.6 m) to -0.67 (21.5 m) in the gabbroic diorite part, followed by a sharp increase in the lower section, with values between -0.12 and 0.06. This is consistent with the trends of both the CIA and PIA. τ_{Ca} values show a high variability compared with τ_{Na}. The sample from 20.6 m yields a τ value of -0.03, which indicates a slight depletion in Ca, whereas the sample from 21.5 m shows a τ value of 0.17, which suggests a slight enrichment in Ca (Fig. 9b). A similar enrichment also occurs at 23.5 m, which yields a value of 0.13 (Table S5).

The Sr/Ca ratio can be applied as a parameter to distinguish different phases of diagenetic fluids (Berndt et al., 1988; Brandstätter et al., 2018). To figure out the source of Ca, the Sr–CaO diagram is applied (Fig. 9a). The ratios of Sr/CaO at the top of the gabbroic diorite at depths of 20.6 and 21.5 m show a close relation to the Sr/CaO ratios of the basaltic andesite, and they clearly deviate from the general trend of the gabbroic diorite and the overlying sedimentary rocks. This hints at a chemical overprint of the gabbroic diorite by the overlying basaltic andesite, whereas the Ca in the lower part appears to be primary. The spike in τ_{Ca} at a depth

of 23.5 m can also be explained by porosity data (Weinert et al., 2021), which can be considered as a measure of fracture density and grain disaggregation in igneous rocks. The porosity decreases sharply from 24 % at a depth of 21.5 m to 3 % at 23.6 m (Fig. 9b). This can be explained by the fact that the fractures provided pathways for meteoric water before the Permian basaltic to andesitic lava flow flooded the basement. Ca was leached by meteoric water, transferred downward through these fractures and accumulated around the interface, where the porosity sharply decreases.

Based on K_{corr}, K was depleted during the weathering process in both basaltic andesite and gabbroic diorite. The depletion trend of K from top to the bottom is similar to the trend of Na. In the topmost part of the basaltic andesite, $\tau_{K_{corr}}$ is -0.59 and gradually increases to -0.35 and 0.08 at depths of 14.3 m and 17.8 m, respectively. In the top part of the gabbroic diorite, $\tau_{K_{corr}}$ increases from -0.26 (20.6 m) to -0.23 (21.5 m) followed by a sharp increase to around 0 in the lowest part (Table S5). The τ value trend of K_{corr} is in agreement with macroscopic and microscopic weathering trends, thereby supporting the applicability of the K correction.

In contrast to Ca and Na, elements closely related to clay formation such as K, Rb and Cs show significant enrichment (Fig. 6). In the gabbroic diorite part, the τ values of K, Rb and Cs decrease from 2.5 to 0.2, from 5.4 to 0.5 and from 19.8 to 2.3 from top to bottom, respectively. Similarly, they decrease in the basaltic andesite from 4.2 to -0.4, from 5.5 to -0.4 and from 8.4 to 0.2 from top to bottom, respectively.

To search for the origin of this enrichment, correlation diagrams for gabbroic diorite, basaltic andesite and sediments are plotted (Fig. 9c). The linear and close relationships between Cs, Rb and K in the gabbroic diorite and basaltic andesite point to a joint alteration of both, whereas the overlying sediments can be excluded as a source. This is consistent with the conclusion of Molenaar et al. (2015), who claimed that the overlain Permian Rotliegend sediment on Sprendlinger Horst formed a "closed system" and diagenetic fluids did not transfer matter in and out of the system. Palmer and Edmond (1989) claimed that mobile elements such as K, Rb and Cs are very easily extracted by thermal fluids and transferred during hydrothermal activity. In addition to clay transformation, typical minerals formed from hot fluids are observed in thin sections and XRD, such as dolomite accompanied by secondary quartz and adularia (Fig. 3). This observation supports the model of a second alteration that was pervasive through the nonconformity and must have happened during burial diagenesis.

Figure 10 displays the τ_M values for all elements. The large-ion lithophile elements (LILEs), K, Rb and Cs, are removed from the figure due to their strong enrichment which would affect the scaling of all other elements. The remaining LILEs, Sr and Ba, are enriched in the gabbroic diorite but depleted in the basaltic andesite. The enrichment in the gabbroic diorite is most probably associated with diffusive

carbonate precipitation, which is missing in the basaltic andesite.

In both gabbroic diorite and basaltic andesite, the τ values gradually increase from LREEs to HREEs (Fig. 10). This indicates that the depletion degree from LREEs to HREEs decreases during the alteration process if the same conditions exist. In a study of the weathering of a granodiorite, Nesbitt (1979) showed that REEs are removed by acidic leaching of meteoric water which becomes buffered with depth and loses its etching effect due to rising pH. Moreover, Nesbitt (1979) proposed that the fractionation of LREEs and HREEs may be controlled by the mineral type. Kaolinite and illite are favorable for LREEs, whereas vermiculite, Fe–Ti oxyhydroxides, relict hornblende and biotite are more favorable for HREEs. In our study, the decreasing depletion degree from LREEs to HREEs in both weathering profiles also indicates that LREEs are more mobile than HREEs in the same acid weathering environment. Moreover, REE fractionation of the gabbroic diorite is less systematic from the top down compared with the basaltic andesite (Fig. 10b). By comparison with rock textures, we assume that this is due to physical fracturing and more heterogeneous chemical alteration in the basement. The strongly depleted samples at depths of 20.6 and 22.5 m are close to fracture zones and possibly more affected by leaching. In contrast, the enriched samples from depths of 21.5 and 23.5 m do not have macro-fractures. This can be explained by acidic meteoric water that used the pathways provided by the macro-fractures in the topmost part of the gabbroic diorite. REEs in the fracture zone were leached, transported downward, and accumulated around the interface of macro-fracture- and macro-fracture-free zone. This is comparable to the behavior of Ca.

The high-field-strength elements (HFSEs), Zr, Nb, Hf, Ta and Th, are expected to be immobile. In the gabbroic diorite, the τ values scatter significantly for specific elements within single samples. The samples from depths of 21.5 and 23.5 m show mostly enriched values as well as Pb and U, which is in line with REEs. Other element shifts appear to be controlled by heterogeneous conservation and alteration of specific minerals due to the fractured and granular texture of the rock. The depletion of Pb and U can be well explained by oxidation during weathering into the mobile species Pb^{6+} and U^{4+}, respectively, and subsequent leaching by meteoric water. In addition, from LILEs to HFSEs, the overall depletion degree decreased in both the basaltic andesite and gabbroic diorite part during the alteration process.

5.3 Burial diagenesis and its implications for weathering intensity evaluation

In addition to correcting the alteration trend, the A–CN–K diagram can also be used to kinetically predict the primary weathering products of plutonic and volcanic rocks (Nesbitt and Young, 1984; Panahi et al., 2000). In this case, this concept is applied to differentiate surface weathering from burial

diagenesis by comparing the remaining secondary minerals in the profile with the theoretical weathering products.

Due to the chemical composition restriction, rock types that contain only minor amounts of K tend to be weathered directly by forming smectite and kaolinite instead of illite regardless of the climate (Nesbitt and Young, 1989). In our case, both gabbroic diorite and basaltic andesite contain minor K. However, secondary minerals mainly consist of illite which makes metasomatic addition of this element during burial diagenesis highly probable (Fedo et al., 1995). As discussed in Sect. 5.2, K metasomatism is possibly promoted by hydrothermal fluids. According to the A–CN–K diagram (Fig. 11), the initial weathering products of the gabbroic diorite should have mainly consisted of smectite, and a small quantity of kaolinite is expected in the top part (20.6–21.5 m). For the basaltic andesite (13.9 m), kaolinite with a small portion of smectite is expected, whereas smectite should be dominant in the lower part. ESEM (environment scanning electron microscopy) indicated kaolinite in two morphologies: vermiform (Fig. 2h) and booklet form (Fig. 2i). According to Chen et al. (2001) and Erkoyun and Kadir (2011), vermiform kaolinite is favored during the in situ formation of kaolinite, whereas the euhedral booklet form is favored during autogenic diagenesis (e.g., Bauluz et al. (2008). Kaolinite formed by chemical weathering is always more anhedral (Bauluz et al., 2008; Varajao et al., 2001); therefore, the influence of subrecent surface-related weathering can be excluded in our case. Based on the XRD results of the gabbroic diorite (Fig. 3), the remaining mineral in the topmost part (13.9 m) of the basaltic andesite is I–S, which can be explained by the conversion of kaolinite and smectite into I–S.

Na and Ca, as needed for the I–S formation, may originate from the original smectite or from diagenesis fluids. The τ values of Na and Ca in the topmost part are -0.99 and -0.93, respectively; therefore, the influence on the CIA and PIA values for evaluating the weathering intensity is negligible. The remaining secondary mineral in the lower part (14.3–19.3 m) is illite, which can be explained by the conversion of smectite into illite. During the conversion from smectite into illite, Ca and Na will be further depleted. The depletion of these elements will surely increase the CIA and PIA values. Due to the higher content of weathering products (smectite), more Ca and Na will be lost. The influence on the CIA and PIA values will also be more evident. Therefore, in this case, due to the low content of original weathering products, the depletion of Ca and Na content should be limited, thereby resulting negligible effects on the CIA and PIA values. Similar to the basaltic andesite, in the gabbroic diorite, the first secondary minerals formed by weathering were predominantly smectite according to the A–CN–K diagram. During the overprint of diagenesis, the smectite was transformed into I–S in the topmost part (20.6–21.5 m); in the lower part (22.5–28.5 m), the smectite was all transformed into illite. Hence, the Ca and Na should be depleted and the CIA and PIA should increase. In
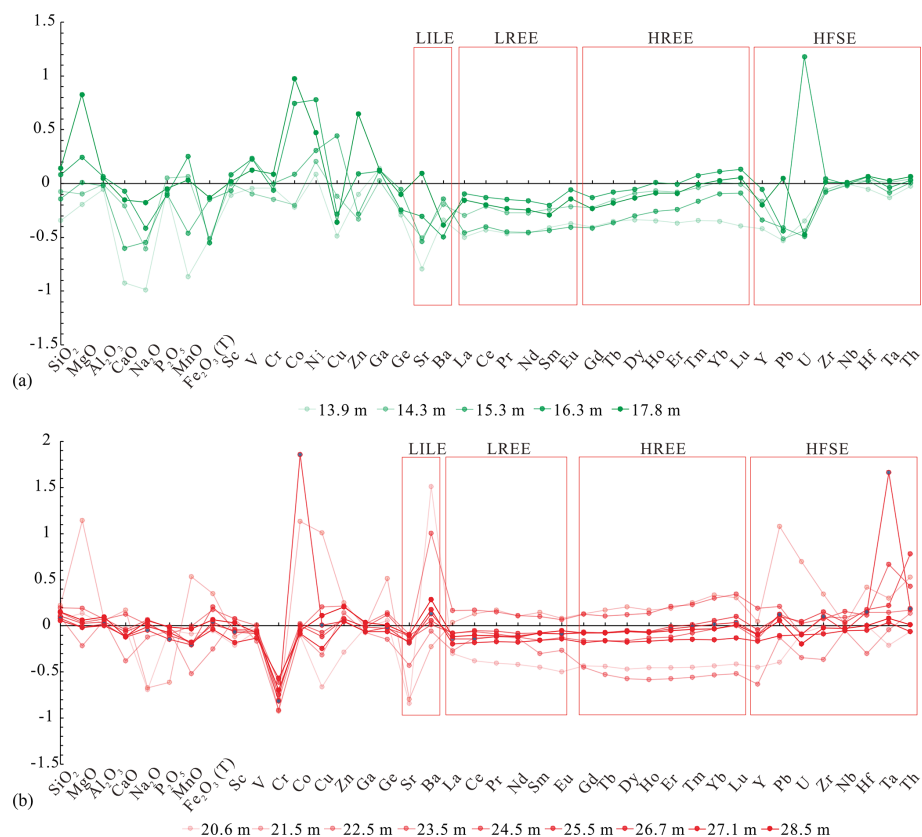
Figure 10. τ value features of basaltic andesite **(a)** and gabbroic diorite **(b)** in the GA1 well.
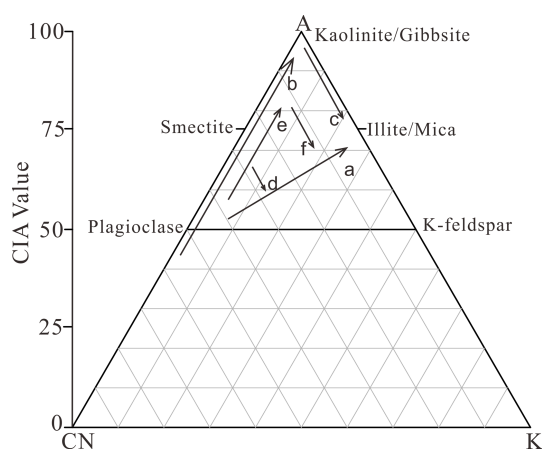
Figure 11. Theoretical weathering trend during burial diagenesis (Fedo et al., 1995): "a" is the observed weathering trend for both basaltic andesite and gabbroic diorite, "b" is the theoretical weathering trend for basaltic andesite, "c" is the K-metasomatism trend of the topmost basaltic andesite, "d" is the K-metasomatism trend of the lower part of basaltic andesite, "e" is the theoretical weathering trend for gabbroic diorite and "f" is the K-metasomatism trend for gabbroic diorite.

the topmost part, this influence should be highest and should decrease with the decreasing content of the secondary minerals towards the lower part. In both basaltic andesite and gabbroic diorite, the illitization makes K addition from outside the system necessary, most probably by fluid migration through fractures. The smectite resulting from weathering in the gabbroic diorite would have been altered to pure illite in the presence of sufficient K. As we observe a high amount of I–S, the K supply was not sufficient to alter the smectite completely to illite in the topmost part of the gabbroic diorite (20.6–21.5 m). A similar mineral content pattern also exists in the basaltic andesite. The illite in the lower part (14.3–16.3 m) was most probably transformed from smectite. However, the K supply was not high enough in the topmost part where I–S and residual kaolinite are dominant (13.9 m) (Fig. 3).

5.4 Implications for paleoclimate

The occurrence of weathering products, such as illite, smectite and kaolinite, can be applied as a useful tool to assess the paleoclimate (Clift et al., 2014; Raucsik and Varga, 2008; Singer, 1988). However, caution should be used when working with these parameters as clay minerals may be overprinted by transformation or neoformation during burial dia-

genesis, and there is also the restriction due to the geochemical composition of rock type, as discussed in Sect. 5.3. It follows that, when the clay minerals in the sedimentary rocks are investigated to assess paleoclimatic conditions, the lithology of the source rocks should be considered. In particular, for the weathering profile of the igneous rock, all of the involved processes mentioned above will lead to misjudgments regarding the paleoclimate conditions if working with raw data. Taking this study as an example and interpreting the original data from XRD and SEM analyses, I–S clay minerals would indicate a subhumid climate with prominent dry seasons (Raucsik and Varga, 2008; Singer, 1988). For the deeper parts of both basaltic andesite and gabbroic diorite, the clay minerals are dominated by illite, pointing to a cold or dry climate. According to this information, the profile would suggest that the climate alternated twice from a cold and dry climate to a seasonal and alternating wet and dry climate. However, due to the limited K availability, the dominant illite in gabbroic diorite and basaltic andesite must be a product of a diagenetic overprint. When correcting the A–CN–K diagram, the primary weathering product in the topmost part of the gabbroic diorite must have been smectite with negligible illite and possibly a small quantity of kaolinite (20.6–21.5 m). Furthermore, smectite can also not be applied to evaluate the paleoclimatic conditions in this case due to the K limitation of the lithology.

Although the CIA and PIA values may be misleading sometimes, they display the alteration intensity of the gabbroic diorite well, with much higher values in the topmost part (20.6–21.5 m). However, a related tendency of HFSEs is nonexistent (Fig. 6b). Due to leaching, these immobile elements are expected to become indirectly enriched, which is not observed. HFSE values and τ values of representative LILEs, such as Na and Sr, show a positive correlation with porosity data, which suggests that the intensity of the leaching process was more dominated by the porosity formed by intense physical weathering than by other factors, such as the climate shifting to more humid conditions.

Correction of the A–CN–K diagram for the basaltic andesite section suggests that primary products of the altered basaltic andesite were dominated by kaolinite in the topmost part (13.9 m) and mainly by smectite in the lower part. Again, smectite cannot be applied as a climate parameter due to the restriction of the K content in basaltic andesite. Similar to the gabbroic diorite section, the CIA and PIA values, the mineral abundances and the petrographic features significantly change between the topmost part (13.9 m) and the lower part (14.3–19.3 m). In contrast to the gabbroic diorite, however, the relative content of high-field-strength elements (HFSEs), such as Nb, Ta, Zr, Hf and Ti, are all drastically shifted between the topmost part (13.9 m) and the lower part (Fig. 6a). The abnormal relative concentrations of these elements in the topmost part indicate more depletion of other relatively more mobile elements, which is confirmed by the τ value of Na and Ca. All parameters together, i.e., the CIA, PIA, rela-

tive content of clay mineral types (additional kaolinite in the topmost part), and petrologic features indicate that the climate changed to humid conditions during basalt weathering. Moreover, the thin saprolite layer demonstrates that surficial weathering only lasted for a short period and that the basalt was rapidly covered by alluvial sediments.

As mentioned in Sect. 5.2, the weathering environment for the basaltic andesite was more acidic than for the gabbroic diorite. The acid present in the weathered profile can be attributed to CO_2 input from the atmosphere or organic acids produced by vegetation. Based on the drill core profile, vegetation was undeveloped at the paleo-surfaces on both the gabbroic diorite and basaltic andesite parts. Hence, the increased acid was probably due to an increase in CO_2 in the atmosphere (Berner, 1992; Neaman et al., 2005), which may also be the reason for the deglaciation event during the Permo-Carboniferous.

# 6   Scenario for alteration at the post-Variscan nonconformity

As the weathering process and the paleoclimate is elucidated, the overall alteration process at the post-Variscan nonconformity can be separated into three subsequent steps (Figs. 12–14). Approximately at the Carboniferous–Permian boundary, the gabbroic diorite was firstly weathered under relatively arid conditions. This included fracturing by physical weathering and moderate chemical weathering. Plagioclase was transformed to smectite with negligible illite (Fig. 12, Eqs. 1–2). Other minerals such as amphibole and biotite were weathered to smectite and chlorite accompanied by the generation of hematite and vermiculite (Fig. 12, Eqs. 3–5). With the beginning of volcanism in the early Permian, the nonconformity was concealed by the basaltic andesite lava flow, which underwent a short but intense period of chemical weathering. Firstly, pyroxene and plagioclase were weathered to vermiculite and smectite (Fig. 13, Eqs. 6–7). Thereafter, more humid conditions initiated increased leaching and smectite was transformed to kaolinite (Fig. 13, Eq. 8). During these two stages, elements such as Na, Ca and K were depleted from the system, either by export or descendent enrichment in the profile. After a relatively short time interval, the basalt was concealed by sediments and the weathering process terminated. During burial diagenesis, fluids transformed smectite and kaolinite into illite in both gabbroic diorite and basaltic andesite (Fig. 13, Eqs. 9–10). The transformation of smectite to illite led to depletion of Ca and Na as well. This leaching process is accompanied by the formation of accessory minerals such as quartz, dolomite, calcite and adularia (Fig. 14, Eqs. 11–12), which indicate a temperature of around 200 °C (Stimac et al., 2015). Emplacement of calcitic veins is partly coupled with low-temperature migration recrystallization quartz (Fig. 2c), which indicates a temperature of around 300 °C (Stipp et al., 2002). This roughly
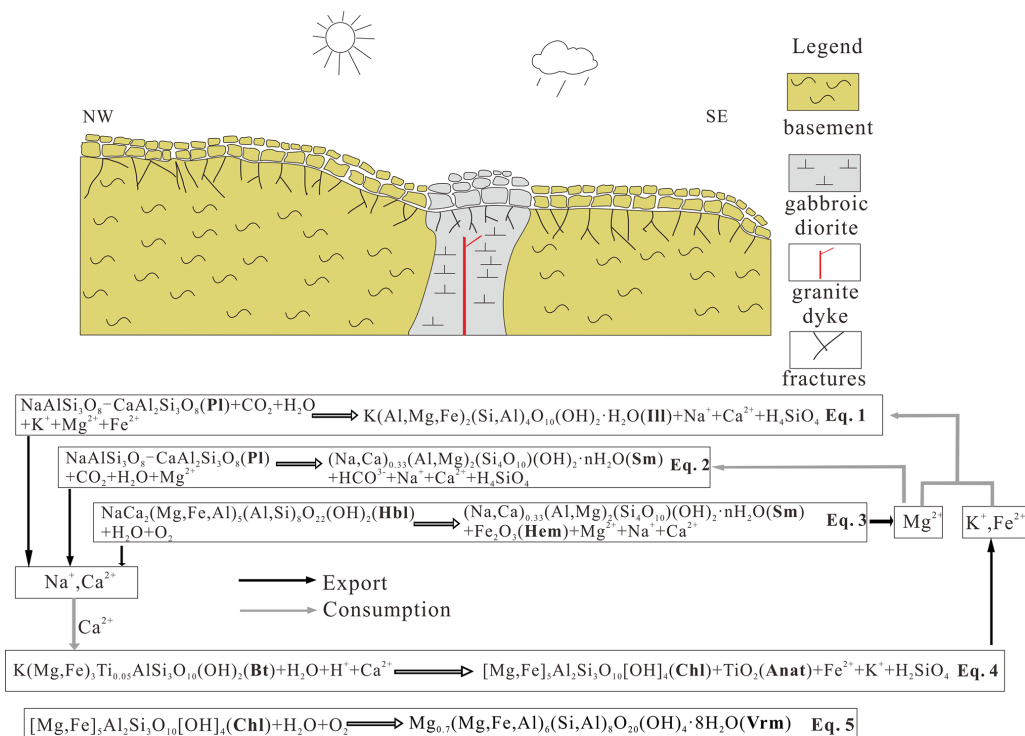
Figure 12. Reconstructed alteration model of the GA1 well in Sprendlinger Horst before volcanic eruption around 300 Ma; The abbreviations used in the figure are as follows: Anat – anatase, Bt – biotite, Chl – chlorite, Hbl – hornblende, Hem – hematite, Ill – illite, Pl – plagioclase, Sm – smectite and Vrm – vermiculite.
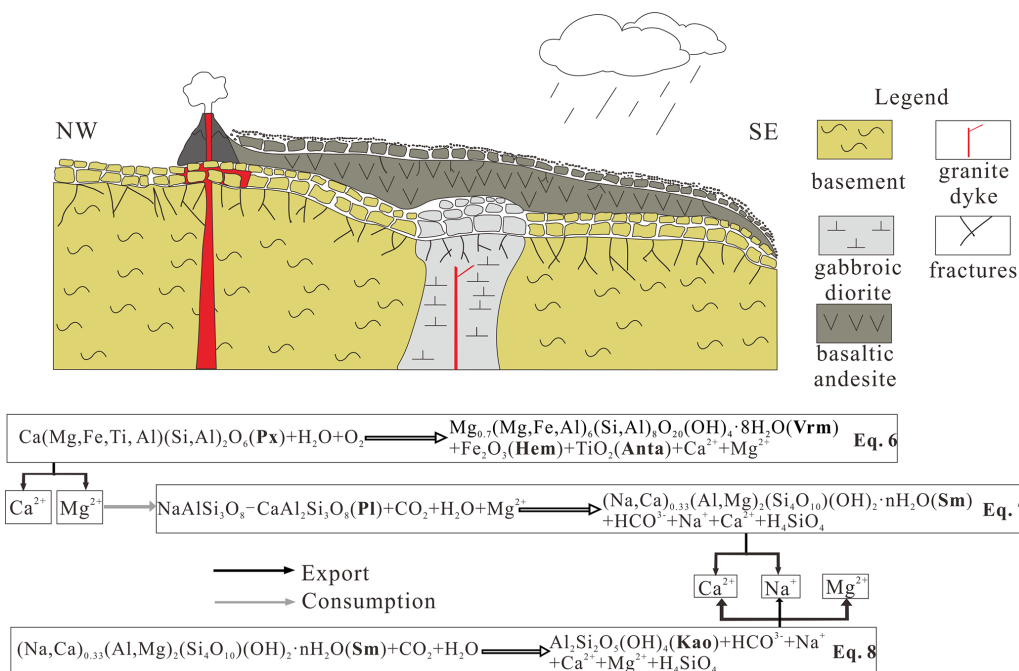
Figure 13. Reconstructed alteration model of the GA1 well in Sprendlinger Horst after volcanic eruption around 290 Ma. Px denotes pyroxene; other abbreviations are given in the caption of Fig. 12.
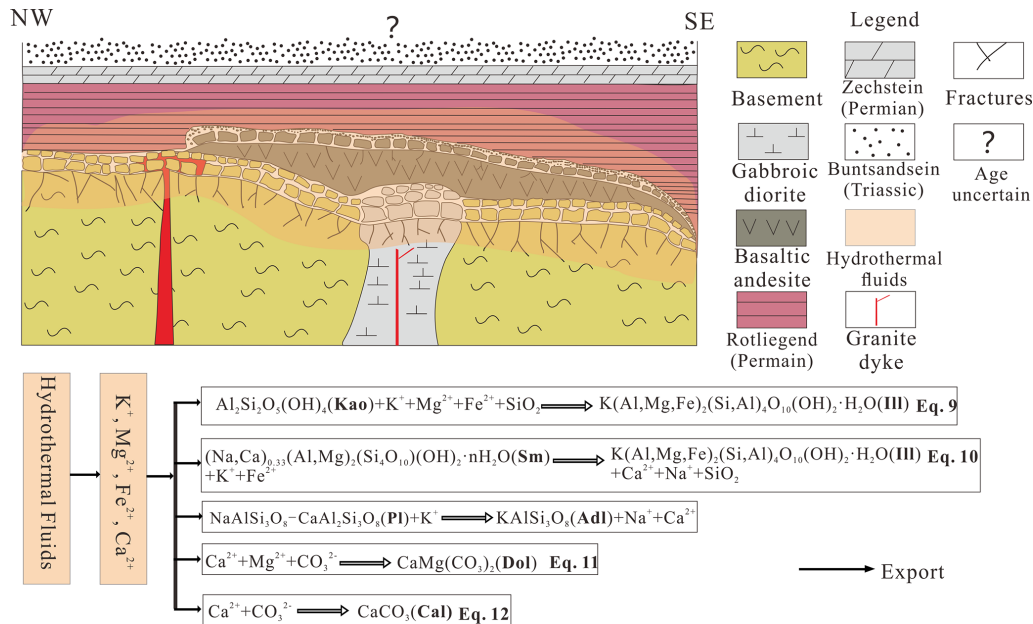
Figure 14. Reconstructed alteration model of the GA1 well in Sprendlinger Horst during burial in the Jurassic and Cretaceous. Adl denotes adularia; other abbreviations are given in the caption of Fig. 12.

coincides with temperatures from thermochronological apatite fission track studies in the surrounding basement of the Odenwald that indicate heating of up to more than $130\,°C$ before 80–105 Ma and homogenization temperatures from fluid inclusions in hydrothermal veins of up to ca. $290\,°C$ (Wagner et al., 1990; Burisch et al., 2017). Subsidence ceased in the uppermost Jurassic, as evident from surrounding sedimentary sequences in southern Germany. Relative stability can be expected until the early Cenozoic, when the European Cenozoic Rift System was initiated and also formed the Sprendlinger Horst (Ziegler et al., 2004). Since the Eocene, the Mesozoic sedimentary cover of the Sprendlinger Horst has been subsequently removed. Most probably, exhumation of the basement did not take place before the upper Miocene (Sissingh, 2003). A further pulse of exhumation is proven for the Middle to Late Pleistocene (Lang, 2007).

7 Conclusions

A combined study of mineralogy, petrography and geochemistry was performed on a drill core that penetrates the post-Variscan nonconformity on the Sprendlinger Horst (southwestern Germany). The aim of this study was to elucidate rock alteration at and across the nonconformity and to disentangle surficial weathering and its overprint by burial diagenesis. The unconformity is covered by a Permian lava flow followed by alluvial sediments of the Rotliegend. This allows for the study of two different lithologies and two subsequent periods of surficial weathering as well as the burial diagenesis affecting both in a later stage. The crystalline basement

is composed of a gabbroic diorite, whereas the lava flow is a basaltic andesite.

In the gabbroic diorite, mineralogical and geochemical parameters show a gradual alteration trend with a maximum depth of around 10 m, whereas the andesitic basalt shows a shallower and more intense alteration with complete chemical alteration in the topmost part. Chemical alteration goes along with physical alteration which is evident from the fracture density. The different alteration steps were separated using thin section analysis, clay mineralogy and geochemistry. In addition, the trends of the A–CN–K diagram and element transfer ratios were used to determine pristine rock compositions.

Surficial weathering of both gabbroic diorite and basaltic andesite are all indicated by petrographic characteristics, increasing abundance of secondary minerals, increasing CIA and PIA values, and enrichment of immobile HFSEs due to the leaching process. In the gabbroic diorite, ubiquitous now filled fractures with a width of around 1 cm in the upmost part (20.6–21.4 m) suggest intense physical weathering combined with chemical weathering, preferentially along these fractures. The corrected clay mineral composition yields smectite with negligible illite and possibly a small quantity of kaolinite, pointing to an arid climate. Physical weathering in the basaltic andesite is much weaker compared with the gabbroic diorite. An overprint by burial diagenesis is indicated by K metasomatism, clay mineral transformation and neoformation of minerals, as well as an enrichment of K, Rb and Cs in the alteration zone. In both the gabbroic diorite and andesitic basalt, the primary weathering products such

as smectite and kaolinite were transformed into illite, and this will also have some influences on the evolution of weathering intensity.

At both nonconformities, distinct gradients from the top downward demonstrate that surficial weathering is the major alteration process. During burial diagenesis, fluids preferentially percolated along the post-Variscan nonconformity and at the basalt–sediment boundary, due to a higher permeability. This led to clay mineral transformation and some neoformation of minerals, but it did not change the alteration pattern. Deeper parts of both parent rocks are pristine and are not affected by surficial weathering nor by fluids during burial diagenesis.

Our case study shows that surface weathering in the past is a primary control on the petrography and geochemistry and also guides fluids through the system during burial diagenesis. Moreover, we could demonstrate that the formation of the saprolite zone depends on rock composition, climatic conditions and the duration of the process. Our results have implications for paleoclimatic and burial diagenetic studies. In order to separate hypergene and supergene alteration, we provide a workflow for nonconformities and shed light on the use of paleo-weathering surfaces for paleoclimate research.

References

Anderson, S. P., Dietrich, W. E., and Brimhall, G. H.: Weathering profiles, mass-balance analysis, and rates of solute loss: Linkages between weathering and erosion in a small, steep catchment, Geol. Soc. Am. Bull., 114, 1143–1158, https://doi.org/10.1130/0016-7606(2002)114<1143:wpmbaa>2.0.co;2, 2002.

Babechuk, M. G., Widdowson, M., Murphy, M., and Kamber, B. S.: A combined Y/Ho, high field strength element (HFSE) and Nd isotope perspective on basalt weathering, Deccan Traps, India, Chem. Geol., 396, 25–41, https://doi.org/10.1016/j.chemgeo.2014.12.017, 2015.

Bauluz, B., Mayayo, M. J., Yuste, A., and González López, J. M.: Genesis of kaolinite from Albian sedimentary deposits of the Iberian Range (NE Spain): analysis by XRD, SEM and TEM, Clay Miner., 43, 459–475, https://doi.org/10.1180/claymin.2008.043.3.10, 2008.

Becker, A., Schwarz, M., and Schäfer, A.: Lithostratigraphische Korrelation des Rotliegend im östlichen Saar-Nahe-Becken (Lithostratigraphic Correlation of the Rotliegend in the eastern Saar-Nahe Basin), Jber. u. Mitt. Oberrhein. Geol. Vereins, 94, 105–133, https://doi.org/10.1127/jmogv/94/2012/105, 2012.

Behrmann, J. H., Ziegler, P. A., Schmid, S. M., Heck, B., and Granet, M.: The EUCOR-URGENT project, Upper Rhine Graben: Evolution and neotectonics, Int. J. Earth Sci., 94, 505–506, https://doi.org/10.1007/s00531-005-0513-0, 2005.

Berndt, M. E., Seyfried, W. E., and Beck, J. W.: Hydrothermal alteration processes at midocean ridges: experimental and theoretical constraints from Ca and Sr exchange reactions and Sr isotopic ratios, J. Geophys. Res.-Sol. Ea., 93, 4573–4583, https://doi.org/10.1029/JB093iB05p04573, 1988.

Berner, R. A.: Weathering, plants, and the long-term carbon cycle, Geochim. Cosmochim. Ac., 56, 3225–3231, https://doi.org/10.1016/0016-7037(92)90300-8, 1992.

Bons, P. D., Fusswinkel, T., Gomez-Rivas, E., Markl, G., Wagner, T., and Walter, B.: Fluid mixing from below in unconformity-related hydrothermal ore deposits, Geology, 42, 1035–1038, https://doi.org/10.1130/G35708.1, 2014.

Borrelli, L., Perri, F., Critelli, S., and Gullà, G.: Characterization of granitoid and gneissic weathering profiles of the Mucone River basin (Calabria, southern Italy), Catena, 113, 325–340, https://doi.org/10.1016/j.catena.2013.08.014, 2014.

Brandstätter, J., Kurz, W., Richoz, S., Cooper, M. J., and Teagle, D. A. H.: The Origin of Carbonate Veins Within the Sedimentary Cover and Igneous Rocks of the Cocos Ridge: Results From IODP Hole U1414A, Geochem. Geophy. Geosy., 19, 3721–3738, https://doi.org/10.1029/2018GC007729, 2018.

Burisch, M., Gerdes, A., Walter, B. F., Neumann, U., Fettel, M., and Markl, G.: Methane and the origin of five-element veins: Mineralogy, age, fluid inclusion chemistry and ore forming processes in the Odenwald, SW Germany, Ore Geol. Rev., 81, 42–61, https://doi.org/10.1016/j.oregeorev.2016.10.033, 2017.

Catuneanu, O.: Principles of sequence stratigraphy, edn. 1, Elsevier Science & Technology, Oxford, United Kingdom, 388 pp., 1996.

Chen, P. Y., Wang, M. K., and Yang, D. S.: Mineralogy of dickite and nacrite from Northern Taiwan, Clay. Clay Miner., 49, 586–595, https://doi.org/10.1346/CCMN.2001.0490608, 2001.

Clift, P. D., Wan, S., and Blusztajn, J.: Reconstructing chemical weathering, physical erosion and monsoon intensity since 25 Ma in the northern South China Sea: A review of competing proxies, Earth-Sci. Rev., 130, 86–102, https://doi.org/10.1016/j.earscirev.2014.01.002, 2014.

Dill, H. G.: Authigenic heavy minerals a clue to unravel supergene and hypogene alteration of marine and continental sediments of Triassic to Cretaceous age (SE Germany), Sediment. Geol., 228, 61–76, https://doi.org/10.1016/j.sedgeo.2010.04.006, 2010.

Dörr, W. and Stein, E.: Precambrian basement in the Rheic suture zone of the Central European Variscides (Odenwald), Int. J. Earth Sci., 108, 1937–1957, https://doi.org/10.1007/s00531-019-01741-7, 2019.

Erkoyun, H. and Kadír, S.: Mineralogy, micromorphology, geochemistry and genesis of a hydrothermal kaolinite deposit and altered Miocene host volcanites in the Hallaçlar area, Uşak, western Turkey, Clay Miner., 46, 421–448, https://doi.org/10.1180/claymin.2011.046.3.421, 2011.

Fedo, C. M., Wayne Nesbitt, H., and Young, G. M.: Unraveling the effects of potassium metasomatism in sedimentary rocks and paleosols, with implications for paleoweathering conditions and provenance, Geology, 23, 921–924, https://doi.org/10.1130/0091-7613(1995)023<0921:uteopm>2.3.co;2, 1995.

Gardner, F. J.: Relationship of unconformities to oil and gas accumulation, AAPG Bull., 24, 2022–2031, https://doi.org/10.1306/3D933278-16B1-11D7-8645000102C1865D, 1940.

Gates-Rector, S. D. and Blanton, T. N.: The Powder Diffraction File: A Quality Materials Characterization Database, Powder Diffraction, 34, 352–360, https://doi.org/10.1017/S0885715619000812, 2019 (PDF-2 and PDF-4 files available at: https://www.icdd.com/pdf-2/ and https://www.icdd.com/pdf-4-minerals/).

Henk, A.: Subsidenz und Tektonik des Saar-Nahe-Beckens (SW-Deutschland), Geol. Rdsch., 82, 3–19, https://doi.org/10.1007/BF00563266, 1993.

Henk, R. A.: Late Variscan exhumation histories of the southern Rhenohercynian Zone and western Mid-German Crystalline

Rise: results from thermal modeling, Geol. Rdsch., 84, 578–590, https://doi.org/10.1007/BF00284522, 1995.

Jian, X., Zhang, W., Liang, H., Guan, P., and Fu, L.: Mineralogy, petrography and geochemistry of an early Eocene weathering profile on basement granodiorite of Qaidam basin, northern Tibet: Tectonic and paleoclimatic implications, Catena, 172, 54–64, https://doi.org/10.1016/j.catena.2018.07.029, 2019.

Kirsch, H., Kober, B., and Lippolt, H. J.: Age of intrusion and rapid cooling of the Frankenstein gabbro (Odenwald, SW-Germany) evidenced by ^{40}Ar/^{39}Ar and single-zircon ^{207}Pb/^{206}Pb measurements, Geol. Rundsch., 77, 693–711, https://doi.org/10.1007/BF01830178, 1988.

Korsch, R. J. and Schzfer, A.: Geological interpretation of DEKORP deep seismic reflection profiles 1C and 9N across the Variscan Saar-Nahe Basin, southwest Germany, Tectonophysics, 191, 127–146, https://doi.org/10.1016/0040-1951(91)90236-L, 1991.

Kroner, U., Hahn, T., Romer, R. L., and Linnemann, U.: The variscan orogeny in the saxo-thuringian zone – Heterogenous overprint of Cadomian/Paleozoic Peri-Gondwana crust, in: Special Paper of the Geological Society of America, Geological Society of America, McLean, Virginia, American, Geological Society of America, 153–172, https://doi.org/10.1130/2007.2423(06), 2007.

Lang, S.: Die geologische Entwicklung der Hanau-Seligenstädter Senke (Hessen, Bayern), Ph.D. thesis, Department of Materials and Earth Sciences, Technische Universität Darmstadt, Germany, 97 pp., 2007.

Lippolt, H. J. and Hess, J. C.: Isotopic evidence for the stratigraphic position of the Saar-Nahe Rotliegend volcanism, I: ^{40}Ar/^{40}K and ^{40}Ar/^{39}Ar investigations, Neues Jahrb. Geol. P.-M., 12, 713–730, https://doi.org/10.1127/njgpm/1983/1983/713, 1983.

Marell, D.: Das Rotliegende zwischen Odenwald und Taunus, Hessisches Landesamt für Bodenforschung, Wiesbaden, Germany, 128 pp., available at: https://katalog.ub.uni-heidelberg.de/cgi-bin/titel.cgi?katkey=66459799 (last access: 19 May 2021), 1989.

Matte, P.: Accretionary history and crustal evolution of the Variscan belt in Western Europe, Tectonophysics, 196, 309–337, https://doi.org/10.1016/0040-1951(91)90328-P, 1991.

McCann, T.: The tectonosedimentary evolution of the northern margin of the Carboniferous foreland basin of NE Germany, Tectonophysics, 313, 119–144, https://doi.org/10.1016/S0040-1951(99)00193-6, 1999.

McCann, T., Pascal, C., Timmerman, M. J., Krzywiec, P., López-Gómez, J., Wetzel, A., Krawczyk, C. M., Rieke, H., and Lamarche, J.: Post-Variscan (end Carboniferous-Early Permian) basin evolution in Western and Central Europe, Geol. Soc. Mem., 32, 355–388, https://doi.org/10.1144/GSL.MEM.2006.032.01.22, 2006.

McDonough, W. F. and Sun, S. S.: The composition of the Earth, Chem. Geol., 120, 223–253, https://doi.org/10.1016/0009-2541(94)00140-4, 1995.

McLennan, S. M.: Weathering and Global Denudation, available at: http://www.journals.uchicago.edu/t-and-c (last access: 19 May 2021), 1993.

Mezger, J. E., Felder, M., and Harms, F. J.: Kristallingesteine in den maarablagerungen von Messel: Schlüssel zum verständnis der geometrien der messel-störungszone und des vulka-

nschlots und der posteruptiven beckenentwicklung, Z. Dtsch. Ges. Geowiss., 164, 639–662, https://doi.org/10.1127/1860-1804/2013/0034, 2013.

Middelburg, J. J., Van Der Weijden, C. H., and Woittiez, J. R. W.: Chemical processes affecting the mobility of major, minor and trace elements during weathering of granitic rocks, Chem. Geol., 68, 253–273, https://doi.org/10.1016/0009-2541(88)90025-3, 1988.

Middlemost, E. A. K.: Naming materials in the magma/igneous rock system, Earth-Sci. Rev., 37, 215–224, https://doi.org/10.1016/0012-8252(94)90029-9, 1994.

Molenaar, N., Felder, M., Bär, K., and Götz, A. E.: What classic greywacke (litharenite) can reveal about feldspar diagenesis: An example from Permian Rotliegend sandstone in Hessen, Germany, Sediment. Geol., 326, 79–93, https://doi.org/10.1016/j.sedgeo.2015.07.002, 2015.

Neaman, A., Chorover, J., and Brantley, S. L.: Implications of the evolution of organic acid moieties for basalt weathering over geological time, Am. J. Sci., 305, 147–185, https://doi.org/10.2475/ajs.305.2.147, 2005.

Nesbitt, H. W.: Mobility and fractionation of rare earth elements during weathering of a granodiorite, Nature, 279, 206–210, https://doi.org/10.1038/279206a0, 1979.

Nesbitt, H. W. and Markovics, G.: Weathering of granodioritic crust, long-term storage of elements in weathering profiles, and petrogenesis of siliciclastic sediments, Geochim. Cosmochim. Acta, 61, 1653–1670, https://doi.org/10.1016/S0016-7037(97)00031-8, 1997.

Nesbitt, H. W. and Young, G. M.: Early proterozoic climates and plate motions inferred from major element chemistry of lutites, Nature, 299, 715–717, https://doi.org/10.1038/299715a0, 1982.

Nesbitt, H. W. and Young, G. M.: Prediction of some weathering trends of plutonic and volcanic rocks based on thermodynamic and kinetic considerations, Geochim. Cosmochim. Ac., 48, 1523–1534, https://doi.org/10.1016/0016-7037(84)90408-3, 1984.

Nesbitt, H. W. and Young, G. M.: Formation and diagenesis of weathering profiles, J. Geol., J. Geol., 97, 129–147, https://doi.org/10.1086/629290, 1989.

Palmer, M. R. and Edmond, J. M.: Cesium and rubidium in submarine hydrothermal fluids: evidence for recycling of alkali elements, Earth Planet Sci Lett., 95, 8–14, https://doi.org/10.1016/0012-821X(89)90163-5, 1989.

Panahi, A., Young, G. M., and Rainbird, R. H.: Behavior of major and trace elements (including REE) during Paleoproterozoic pedogenesis and diagenetic alteration of an Archean granite near Ville Marie, Québec, Canada, Geochim. Cosmochim. Acta, 64, 2199–2220, https://doi.org/10.1016/S0016-7037(99)00420-2, 2000.

Parrish, J. T.: Climate of the supercontinent Pangea, J. Geol., 101, 215–233, https://doi.org/10.1086/648217, 1993.

Parrish, J. T.: Geologic Evidence of Permian Climate, in: The Permian of Northern Pangea: Paleogeography, Paleoclimates, Stratigraphy, edited by: Scholle, P. A., Peryt, T. M., and Ulmer-Scholle, D. S., Springer Berlin Heidelberg, Berlin, Heidelberg, Germany, 53–61, 1995.

Patino, L. C., Velbel, M. A., Price, J. R., and Wade, J. A.: Trace element mobility during spheroidal weathering of basalts and an-desites in Hawaii and Guatemala, Chem. Geol., 202, 343–364, https://doi.org/10.1016/j.chemgeo.2003.01.002, 2003.

Pearce, J. A.: A User's Guide to Basalto Discriminant Diagrams, Geological Association of Canada, Short Course Notes, edited by: Wyman, D. A., 12, 79–113, 1996.

Petschick, R., Kuhn, G., and Gingele, F.: Clay mineral distribution in surface sediments of the South Atlantic: Sources, transport, and relation to oceanography, Mar. Geol., 130, 203–229, https://doi.org/10.1016/0025-3227(95)00148-4, 1996.

Powell, C. M. A. and Conaghan, P. J.: Plate tectonics and the Himalayas, Earth Planet. Sc. Lett., 20, 1–12, https://doi.org/10.1016/0012-821X(73)90134-9, 1973.

Raucsik, B. and Varga, A.: Climato-environmental controls on clay mineralogy of the Hettangian-Bajocian successions of the Mecsek Mountains, Hungary: An evidence for extreme continental weathering during the early Toarcian oceanic anoxic event, Palaeogeogr. Palaeocl., 265, 1–13, https://doi.org/10.1016/j.palaeo.2008.02.004, 2008.

Roscher, M. and Schneider, J. W.: Permo-Carboniferous climate: Early Pennsylvanian to Late Permian climate development of central Europe in a regional and global context, Geol. Soc. Spec. Publ., 265, 95–136, https://doi.org/10.1144/GSL.SP.2006.265.01.05, 2006.

Schäfer, O.: Tektonik und Sedimentation im kontinentalen Saar-Nahe-Becken ("Strike-lip"-Modell, Karbon-Perm, Westdeutschland), Z. Dtsch. Ges. Geowiss., 162, 127–155, https://doi.org/10.1127/1860-1804/2011/0162-0127, 2011.

Schubert, W., Lippolt, H. J., and Schwarz, W.: Early to Middle Carboniferous hornblende $^{40}Ar/^{39}Ar$ ages of amphibolites and gabbros from the Bergsträsser Odenwald, Miner. Petrol., 72, 113–132, https://doi.org/10.1007/s007100170029, 2001.

Schulmann, K., Catalán, J. R. M., Lardeaux, J. M., Janoušek, V., and Oggiano, G.: The Variscan orogeny: Extent, timescale and the formation of the European crust, Geol. Soc. Spec. Publ., 405, 1–6, https://doi.org/10.1144/SP405.15, 2014.

Schwarz, M. and Henk, A.: Evolution and structure of the Upper Rhine Graben: Insights from three-dimensional thermomechanical modelling, Int. J. Earth Sci., 94, 732–750, https://doi.org/10.1007/s00531-004-0451-2, 2005.

Singer, A.: Illite in aridic soils, desert dusts and desert loess, Sediment. Geol., 59, 251–259, https://doi.org/10.1016/0037-0738(88)90079-6, 1988.

Sissingh, W.: Tertiary paleogeographic and tectonostratigraphic evolution of the Rhenish Triple Junction, Palaeogeogr. Palaeocl., 196, 229–263, https://doi.org/10.1016/S0031-0182(03)00320-1, 2003.

Staude, S., Göb, S., Pfaff, K., Ströbele, F., Premo, W. R., and Markl, G.: Deciphering fluid sources of hydrothermal systems: A combined Sr- and S-isotope study on barite (Schwarzwald, SW Germany), Chem. Geol., 286, 1–20, https://doi.org/10.1016/j.chemgeo.2011.04.009, 2011.

Stimac, J., Goff, F., and Goff, C. J.: Intrusion-Related Geothermal Systems, in: The Encyclopedia of Volcanoes, edn. 2, edited by: Haraldur, S., Elsevier, London, Oxford, UK, 799–822, https://doi.org/10.1016/B978-0-12-385938-9.00046-8, 2015.

Stipp, M., Stünitz, H., Heilbronner, R., and Schmid, S. M.: Dynamic recrystallization of quartz: Correlation between natural and experimental conditions, Geol. Soc. Spec. Publ., 200, 171–190, https://doi.org/10.1144/GSL.SP.2001.200.01.11, 2002.

Stollhofen, H.: Facies architecture variations and seismogenic structures in the Carboniferous-Permian Saar-Nahe Basin (SW Germany): evidence for extension-related transfer fault activity, Sediment. Geol., 119, 47–83, https://doi.org/10.1016/S0037-0738(98)00040-2, 1998.

Timar-Geng, Z., Fügenschuh, B., Schaltegger, U., and Wetzel, A.: The impact of the Jurassic hydrothermal activity on zircon fission track data from the southern Upper Rhine Graben area, Schweiz. Miner. Petrog., 84, 257–269, 2004.

Timar-Geng, Z., Fügenschuh, B., Wetzel, A., and Dresmann, H.: Low-temperature thermochronology of the flanks of the southern Upper Rhine Graben, Int. J. Earth Sci., 95, 685–702, https://doi.org/10.1007/s00531-005-0059-1, 2006.

Varajao, A. F. D. C., Gilkes, R. J., and Hart, R. D.: The relationships between kaolinite crystal properties and the origin of materials for a Brazilian kaolin deposit, Clay. Clay Miner., 49, 44–59, https://doi.org/10.1346/CCMN.2001.0490104, 2001.

Vázquez, M., Ramírez, S., Morata, D., Reich, M., Braun, J. J., and Carretier, S.: Regolith production and chemical weathering of granitic rocks in central Chile, Chem. Geol., 446, 87–98, https://doi.org/10.1016/j.chemgeo.2016.09.023, 2016.

von Seckendorff, V., Arz, C., and Lorenz, V.: Magmatism of the late Variscan intermontane Saar-Nahe Basin (Germany): A review, Geol. Soc. Spec. Publ., 223, 361–391, https://doi.org/10.1144/GSL.SP.2004.223.01.16, 2004a.

von Seckendorff, V., Timmerman, M. J., Kramer, W., and Wrobel, P.: New ^{40}Ar/^{39}Ar ages and geochemistry of late Carboniferous-early Permian lamprophyres and related volcanic rocks in the Saxothuringian Zone of the Variscan Orogen (Germany), Geol. Soc. Spec. Publ., 223, 335–359, https://doi.org/10.1144/GSL.SP.2004.223.01.15, 2004b.

Wagner, G. A., Kernphysik, M., and Heidelberg, D.: Crystalline Basement of Middle Europe, Tracks, 17, 277–282, 1990.

Weinert, S., Bär, K., and Sass, I.: Database of petrophysical properties of the Mid-German Crystalline Rise, Earth Syst. Sci. Data, 13, 1441–1459, https://doi.org/10.5194/essd-13-1441-2021, 2021.

Willner, A. P., Massonne, H. J., and Krohe, A.: Tectono-thermal evolution of a part of a Variscan magmatic arc: The Odenwald in the Mid-German Crystalline Rise, Geol. Rundsch., 80, 369–389, https://doi.org/10.1007/BF01829372, 1991.

Zeh, A. and Brätz, H.: Timing of Upper Carboniferous-Permian horst-basin formation and magmatism in the NW Thuringian Forest, central Germany: A review, Geol. Soc. Spec. Publ., 223, 319–334, https://doi.org/10.1144/GSL.SP.2004.223.01.14, 2004.

Zeh, A. and Gerdes, A.: Baltica- and Gondwana-derived sediments in the Mid-German Crystalline Rise (Central Europe): Implications for the closure of the Rheic ocean, Gondwana Res., 17, 254–263, https://doi.org/10.1016/j.gr.2009.08.004, 2010.

Zeh, A. and Will, T. M.: The mid-German crystalline zone, in: Pre-Mesozoic Geology of Saxo-Thuringia – From the Cadomian active margin to the Variscan orogen, edited by: Linnemann, U. and Romer, R. L., Schweozerbart Science Publishers, Stuttgart, Germany, 195–220, 2008.

Zhou, L., Friis, H., Yang, T., and Nielsen, A. T.: Geochemical interpretation of the Precambrian basement and overlying Cambrian sandstone on Bornholm, Denmark: Implications for the weathering history, Lithos, 286–287, 369–387, https://doi.org/10.1016/j.lithos.2017.06.019, 2017.

Ziegler, P. A., Schumacher, M. E., Dèzes, P., van Wees, J. D., and Cloetingh, S.: Post-Variscan evolution of the lithosphere in the Rhine Graben area: Constraints from subsidence modelling, Geol. Soc. Spec. Publ., 223, 289–317, https://doi.org/10.1144/GSL.SP.2004.223.01.13, 2004.